A Grüneisen tensor for rutile and its application to host-inclusion systems

American Mineralogist, Volume 106, pages xxx–xxx, 2021

A Grüneisen tensor for rutile and its application to host-inclusion systems

Kira A. Musiyachenko[1,‡], Mara Murri[2], Mauro Prencipe[3], Ross J. Angel[4,*], and Matteo Alvaro[1,†]

[1]Department of Earth and Environmental Sciences, University of Pavia, Via A. Ferrata, 1 27100 Pavia, Italy
[2]Department of Earth and Environmental Sciences, University of Milano-Bicocca, Piazza della Scienza 4, I-20126 Milano, Italy
[3]Department of Earth Sciences, University of Torino, Via Valperga Caluso 35, 10125 Torino, Italy
[4]IGG CNR, Via Giovanni Gradenigo, 6, 35131 Padova, Italy

Abstract

Rutile is often found as inclusions in garnet, quartz, and several other rock-forming minerals, and it is also a common accessory phase in high-pressure metamorphic rocks. Its relatively simple structure, chemistry, broad *P-T* stability field, and its wide occurrence in nature makes it a candidate for the application of elastic geobarometry. However, thermodynamic studies coupled with observations on natural samples predict that rutile inclusions in garnets should exhibit zero residual pressure. This implies that the rutile inclusions are detached from the inclusion walls in the host garnet after entrapment. We determined the elastic and vibrational properties of rutile via ab initio hybrid Hartree-Fock/Density Functional Theory simulations under different strain states. Our results confirmed the thermodynamic behavior of rutile in garnet and allowed us to determine for the first time the components of the phonon-mode Grüneisen tensors of rutile. We demonstrated that pure rutile inclusions in garnets from metamorphic rocks exhibit no residual strain or stress, consistent with thermodynamic modeling. Nevertheless, there are rutile inclusions in garnet surrounded by optical birefringence haloes, which are indicative of residual inclusion pressures. Careful examination of these show that they contain significant amounts of amphibole, which reduce the elastic moduli of the composite inclusion to less than that of the garnet hosts. A calculation method for the residual pressures of multi-phase inclusions is described.

Keywords: Rutile, Grüneisen tensor, HF/DFT, elastic geobarometry

Introduction

Rutile is a widely distributed mineral in all types of rocks and has a wide range of applications in Earth sciences. It is one of the most important carriers of titanium and high field strength elements (HFSEs: Nb, Ta, Zr, Hf) (e.g., Meinhold 2010). Large rutile crystals usually occur in granitic pegmatites and vein mineralization (e.g., Černý et al. 2007, 2015). More commonly, rutile occurs as an accessory phase, both as inclusions in the rock-forming minerals and within the matrix. Rutile inclusions can have several origins; they can be primary (i.e., igneous or metamorphic, peritectic, xenocrystic) or secondary phases (i.e., hydrothermal alteration; e.g., Carruzzo et al. 2006; Meinhold 2010).

Rutile is already widely used in classical geothermobarometry in a variety of chemical thermometers and barometers (e.g., Ferry and Watson 2007). Moreover, when it occurs as primary inclusions, it also has the potential to provide fundamental information about the pressures and temperatures of entrapment through elastic geobarometry. This provides a different and complementary approach to recover the crystallization conditions of the system, which does not require a chemical equilibrium, but it is based on the elastic interactions between the host-inclusion pair (e.g., Rosenfeld and Chase 1961; Angel et al. 2014b; Alvaro et al. 2020). Because of the contrast in the elastic properties, the host-inclusion system develops non-lithostatic stresses upon exhumation. The residual elastic strain in the inclusion can be determined directly (e.g., from the measured lattice parameters with single-crystal X-ray diffraction) or indirectly from the changes in the wavenumbers of Raman-active phonon modes relative to an unstrained crystal with the phonon-mode Grüneisen approach (Murri et al. 2018; Angel et al. 2019). The remnant inclusion stress is then calculated from the measured strains. In addition, the remnant stress in the inclusion can be detected as birefringence haloes around the inclusion pointing to the fact that the host-inclusion interface and the surrounding host mineral are **{{auth: ok?}}** deformed [i.e., it is subject to strains (Campomenosi et al. 2020)].

In this paper, we present the structure and the Raman spectra of rutile calculated by means of ab initio hybrid Hartree-Fock/Density Functional Theory (HF/DFT) simulations under different strain conditions (i.e., from –2% to +2% covering the expected range of strains for common rutile inclusions) to determine the components of the phonon-mode Grüneisen tensors of rutile. We then discuss the application of elastic geobarometry to garnet-rutile host-inclusion systems.

* E-mail: rossjohnangel@gmail.com, ross.angel@igg.cnr.it **{{ED: Which email address?}}**
† Orcid 0000-0002-6975-3241
‡ Orcid 0000-0002-1614-2201

0003-004X/21/0010–xxx$05.00/DOI: https://doi.org/10.2138/am-2021-2618

Methods

Quantum mechanical calculations

Ab initio hybrid HF/DFT simulations have been performed with the CRYSTAL17 code (Dovesi et al. 2018b) by employing the WC1LYP functional, which is particularly suitable for the correct reproduction of the elastic and vibrational properties of crystals (e.g., Prencipe 2012, 2019; Stangarone et al. 2016). The WC1LYP functional is based on the generalized gradient approximation (GGA) exchange functional WC (Wu and Cohen 2006), mixed with 16% of the exact non-local Hartree-Fock exchange. The functional also includes the LYP correlation contribution (Lee et al. 1988). The grid for the numerical evaluation of the DFT exchange-correlation functionals was chosen by the keyword XXLGRID of the CRYSTAL17 user manual (Dovesi et al. 2018a) and corresponds to a total of 19 394 points in the unit cell. A measure of the numerical accuracy provided by such a grid is the evaluation of the total number of electrons in the unit cell, by the numerical integration of the electron density over the cell volume. For rutile, we obtained 76.00003 electrons out of 76 for the reference volume at the static limit [i.e., 0 GPa and no zero-point and thermal pressures due to vibrational effects included (see Prencipe et al. 2011)]. The localized contracted atomic basis sets used were 8-6411(d311f) and 8-411d11f (Erba and Dovesi 2013; Peintinger et al. 2013) for Ti and O, respectively.

Within the CRYSTAL code, the accuracy in evaluating the Coulomb and Hartree-Fock exchange series is controlled by the keyword TOLINTEG, for which we set the five parameters to 10 (T1, T2, T3, and T4) and 24 (T5) (Dovesi et al. 2014). The diagonalization of the Hamiltonian matrix was performed at 18 independent *k* vectors in reciprocal space (Monkhorst and Pack 1976) by setting the shrinking factor IS to 4 (Dovesi et al. 2014). Cell parameters and fractional coordinates were optimized by analytical gradient methods, as implemented in CRYSTAL17 (Civalleri et al. 2001; Dovesi et al. 2014, 2018b). For hydrostatic simulations, lattice parameters and fractional coordinates were optimized at the WC1LYP level (at the static limit), at pressures of 0, 3, 5, and 10 GPa using the keyword EXTPRESS. Geometry optimization was considered converged when each component of the gradient (TOLDEG parameter in CRYSTAL17) was smaller than 0.00003 Hartree/Bohr and displacements (TOLDEX) were smaller than 0.00012 Bohr with respect to the previous step. For the non-hydrostatic simulations, the cell was fixed at the chosen strain conditions, and only the fractional coordinates were optimized with the keyword ATOMONLY (Civalleri et al. 2001; Dovesi et al. 2014). The chosen values of strains are large enough to provide changes in frequency of vibrational modes that are significantly above the level of the numerical noise in the simulations. These values also cover the range of strains expected to be found in rutile inclusions. All simulations preserved the tetragonal symmetry of rutile. Vibrational wavenumbers of all of the normal modes were calculated at the Γ point within the limit of the harmonic approximation, by diagonalizing a mass-weighted Hessian matrix, whose elements are the second derivatives of the full potential of the crystal with respect to the mass-weighted atomic displacements (Pascale et al. 2004).

Structural and vibrational data for all of the simulations, performed at the static limit, are reported in the Online Materials[1] (CIF). The space group symmetry of rutile, TiO_2, is $P4_2/mnm$ with a primitive unit cell containing six atoms. This gives rise to 18 crystal normal phonons in rutile, three of which are acoustic phonons and have zero wavenumber at the Brillouin-zone center. Hence, the representation of the remaining 15 optic phonons at the center of the Brillouin zone is:

$$\Gamma_{opt} = 1A_{1g} + 1A_{2g} + 1A_{2u} + 1B_{1g} + 1B_{2g} + 2B_{1u} + 1E_g + 3E_u.$$

The A_{2g}, A_{2u}, B_{1u}, and E_u modes are only infrared-active, while the A_{1g} mode is non-polar and only Raman active together with the B_{1g}, B_{2g}, and the doubly degenerate E_g mode. Since rutile is centrosymmetric the transverse and longitudinal optical polarizations of the E_g mode have the same frequency.

Raman spectroscopy

Rutile Raman spectra of both intergranular grains and inclusions in garnet were collected from eclogite sample SL501 from Pohorje Mountains (Eastern Alps, Slovenia; Vrabec et al. 2012). Two reference rutile crystals were measured as standards. One intergranular rutile was measured to have a reference with the same chemical composition as the inclusions. A further crystal of unknown provenance was selected from the mineralogical collection of the Department of Earth and Environmental Sciences at the University of Pavia to have another standard free crystal of rutile.

Raman spectra were collected with a Horiba LabRam HR Evolution spectrometer (holographic gratings of 1800 grooves/mm) equipped with an Olympus BX41 confocal microscope at the controlled temperature of 20(1) °C. Raman spectra were excited by the 532 nm line of a solid-state (YAG) laser. The laser power on the sample surface was ~1–2 mW. The spectrometer was calibrated to the silicon Raman peak at 520.5 cm^{-1}. The spectral resolution was ~2 cm^{-1} and the instrumental reproducibility in determining the peak positions was ~0.5 cm^{-1}. The OriginPro 2018 software package was used for data evaluation. The collected spectra were baseline corrected for the continuum luminescence background and normalized to the acquisition time. Peak positions, full-widths at half maximum (FWHMs), and integrated intensities were determined from fits with pseudo-Voigt functions **{{auth: please advise on italic – p? V?q?}}** [pV = (1 – q)·Lorentz + q·Gauss, where q is the weight coefficient]. The change in the peak position, hereafter Δω (cm^{-1}), is calculated as the difference between the wavenumber of the peak of the sample inclusion crystal (ω_i) and the peak position of the unstrained reference crystal (ω_0) used as the standard. To avoid changes in peak position due to instrumental drift and/or minor changes to room temperature affecting Δω, the unstrained standard of the rutile was measured multiple times per session. The ω_0 values were averaged and then subtracted from the ω_i of the strained inclusions analyzed in between two consecutive standard measurements to obtain Δω.

Results

Structure at the static limit

The structure of rutile consists of chains of TiO_6 octahedra parallel to **c** axis (Fig. 1). Each chain is built by octahedra each of which shares two opposite edges with adjacent octahedra. The structure has one unique titanium and oxygen position and two non-equivalent nearest neighbor Ti-O distances with the longer two (Ti-O_b) oriented perpendicular to the **c**-axis and the shorter four Ti-O_a lying in the <110> plane. Lattice and structural parameters (atomic coordinates, bonds, and angles; Table 1) determined via ab initio simulations at the static limit (0 K, 0 GPa static pressure) are in good agreement with those from Burdett et al. (1987) determined by neutron diffraction measurements at 15 K [Table 1; column "tw-b"—the difference between the results of this work and the results of Burdett et al. (1987), columns "this work" and "b," respectively].

Hydrostatic calculations of the lattice parameters (V/V_0, a/a_0, c/c_0) reproduced correctly the pattern of anisotropy of the

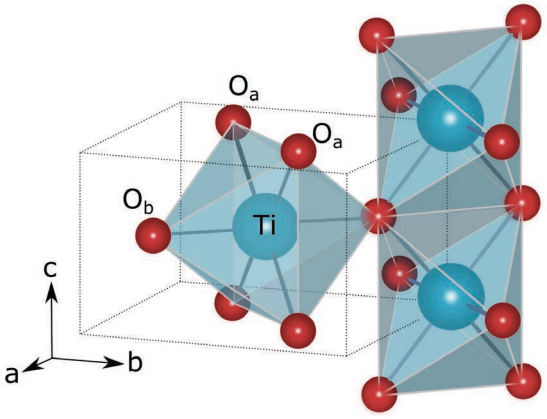

Figure 1. Rutile structure model in three dimensions. Blue spheres in octahedral coordination represent Ti atoms, red spheres represent O atoms. Bonds are represented by dark-gray lines. The unit cell of rutile is indicated by the dashed lines. Structure was drawn with the VESTA software (Momma and Izumi 2008) based on the ab initio calculation at the static limit. (Color online.)

TABLE 1. Lattice parameters, atomic coordinates, bonds, and angles of rutile {{auth: a-f letters ok or should they be bold or italic?}}

	This work	a	b	c	d	e	f	tw-b
T (K)	0	0	15	298	298	298	300	–
Lattice parameters								
a (Å)	4.59867	4.572	4.58666(4)	4.594	4.5924(2)	4.5923(3)	4.499	0.01201
c (Å)	2.95652	2.943	2.95407(3)	2.959	2.9575(2)	2.9576(3)	3.077	0.00245
V (Å^3)	62.52389	61.52	62.15	62.432	62.38(1)	62.37	62.28	0.37389
Atomic coordinates								
O_x	0.30485	0.30400	0.30469(6)	0.30500	0.30499(8)	0.3092(6)	0.30590	0.00016
Bonds and angles								
Ti-O_a (Å)	1.9483	–	1.9459 (3)	–	1.9470(2)	1.930(3)	–	0.0024
Ti-O_b (Å)	1.9826	–	1.9764 (4)	–	1.9808(3)	2.008(4)	–	0.0062
Ti-O-Ti (°)	130.648	–	130.62 (1)	–	130.58 (1)	129.97(9)	–	0.028
O_a-Ti-O_a (°)	81.296	–	81.24 (2)	–	81.16(1)	79.93(18)	–	0.055
Ti-O-Ti (°)	98.704	–	98.76 (2)	–	–	–	–	–0.055
O_b-Ti-O_b (°)	98.704	–	98.76 (2)	–	–	–	–	–0.055

[a] Mitev et al. (2010).
[b] Burdett et al. (1987).
[c] Abrahams and Bernstein (1971).
[d] Sugiyama and Takéuchi (2015).
[e] Henderson et al. (2009).
[f] Lan et al. (2015).

elasticity of rutile, with the **c**-axis being much stiffer than the **a**- and **b**-axes (Figs. 2b and 2c). The zero-pressure bulk modulus determined by fitting the volumes from the hydrostatic simulations against static pressures with a third-order Birch-Murnaghan equation of state (BM3-EoS), is 233.78(24) GPa with the $K' = 4.54(5)$. The calculated bulk modulus is stiffer than that determined by Zaffiro et al. (2019) and Angel et al. (2020) from the available data in the literature [$K_{0T} = 205.14(15)$ GPa, $K' = 6.9(4)$], obtained by using the same EoS, partially because our simulations are performed at the static limit and therefore do not account either for the zero-point pressure nor for thermal pressure that would soften the bulk modulus on passing from 0 to 300 K (Prencipe et al. 2011). In addition, the rutile structure has a soft mode whose effect on the bulk modulus will not be accounted for in our static DFT simulations. The intrinsic anharmonicity of the soft mode would cause a further reduction of the calculated K_{0T}. This effect was observed for the soft mode in quartz (e.g., Demuth et al. 1999; Kimizuka et al. 2003).

Structure under various strain conditions

Under hydrostatic conditions, the structures simulated by HF/DFT show a smooth compression of all structural parameters with increasing pressure (hydrostatic pressure trend is marked by the dotted line in Fig. 3). Figure 3 shows the change of various structural parameters of rutile under non-symmetry-breaking strains. The strain definition used is Lagrangian infinitesimal, and the reference system for the strains coincides with the unit-cell axes. Therefore, $\varepsilon_3 = c/c_0 - 1$ represents the fractional change of the **c** axis relative to the unstrained reference state at zero pressure, with cell parameters a_0 and c_0. To maintain tetragonal symmetry, the strains ε_1 and ε_2 were constrained to be equal, and the contour maps are therefore plotted with $2\varepsilon_1 = \varepsilon_1 + \varepsilon_2$ as the *x*-axis. A negative strain therefore corresponds to a compression of the corresponding axis, and the lower left quadrant of the contour plots represents compression of all three axes of the unit cell of rutile. The top left quadrant represents conditions of shear strain, equivalent to expansion of the **c** axis and isotropic compression in the **a-b** plane. The bottom right quadrant represents the opposite sense of shear strains.

Shortening of the Ti-O bonds with negative ε_1 and ε_3 strains is explained by geometrical orientation of the bonds: Ti-O_b is

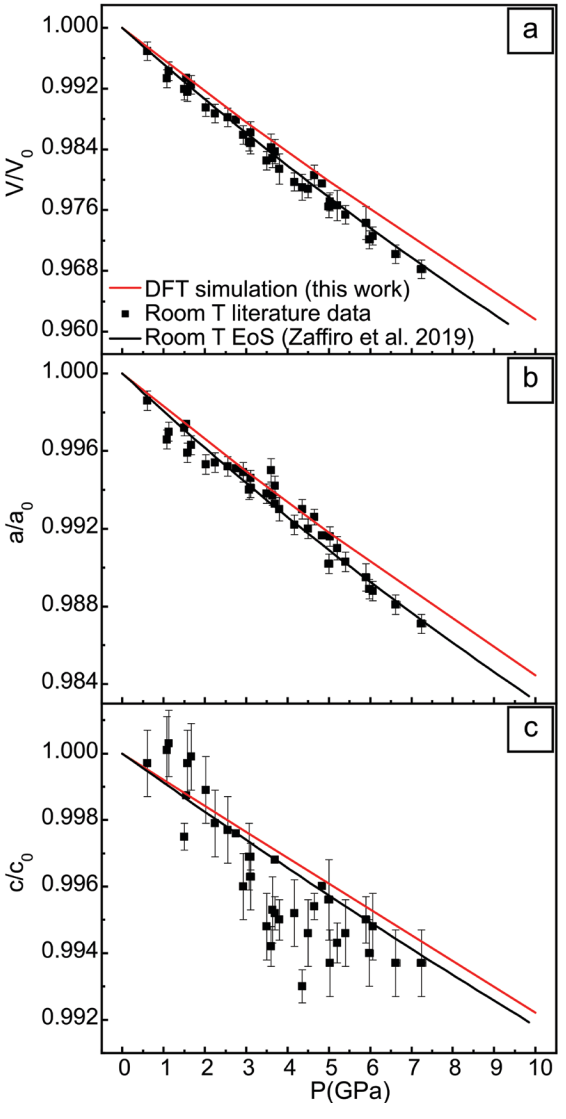

FIGURE 2. Lattice parameters and volume of rutile as a function of pressure. (Color online.)

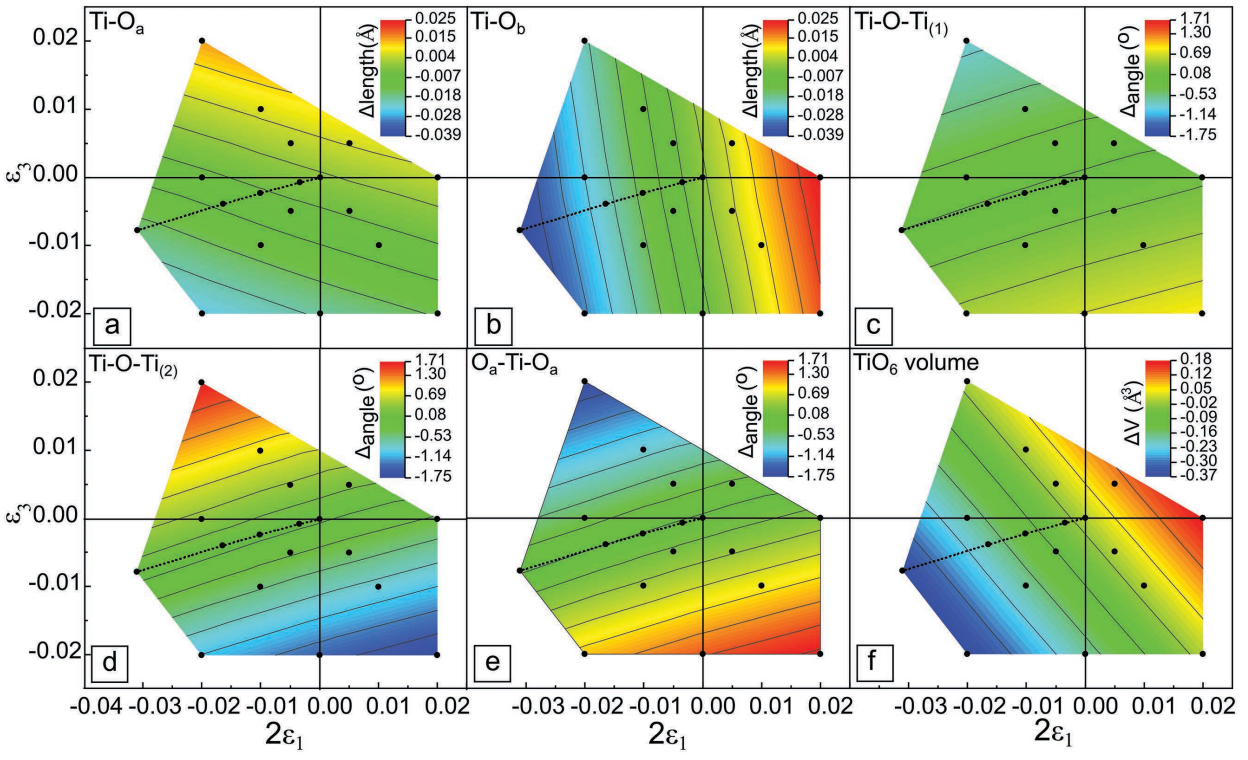

Figure 3. Contour maps of structural parameters of rutile as a function of strains e1 and e3. Strains derived from the hydrostatic pressure simulations lie along the dotted line and represent pressure conditions of 0, 1, 3, 5, and 10 GPa; zero pressure is at the origin of all of these plots. (Color online.)

parallel to the **a-b** plane while Ti-O_a has a smaller angle with the **c** axis (Fig. 1). In contrast, values of the bond angles display a strong dependence on the deviatoric strain with the Ti-O-Ti(1) being the less sensitive, whereas polyhedral volume contours are parallel to the isochors (Fig. 3c). This pattern of structural behavior is similar to that of quartz and zircon (Murri et al. 2019; Stangarone et al. 2019), demonstrating that non-hydrostatic stresses in the most common mineral inclusions found in garnet hosts are mostly accommodated by internal angular distortion and deformation of the polyhedra (i.e., SiO_4 tetrahedra, ZrO_8 polyhedra, and TiO_6 octahedra). These studies show that the dominant structural response of crystal structures under deviatoric stress is shear deformation of the strongly bonded cation-oxygen polyhedra and, where this is allowed by the topology of the structure, as in quartz (Murri et al. 2019), the tilting of the polyhedra with respect to one another.

Raman spectrum

Experimentally determined Raman spectra of rutile consist of four easily detectable bands: one low-intensity sharp peak at 142 cm^{-1} (B_{1g}), a broadband centered at 230 cm^{-1} (multi-phonon interaction process, Porto et al. 1967), a medium-intensity band at 445 cm^{-1} (E_g), and a strong band at 609 cm^{-1} (A_{1g}). Moreover, from the factor-group analysis (see Methods section), one B_{2g} mode is also Raman active. This occurs at 801 cm^{-1}, but it is usually hard to detect due to its very low intensity and broad character (Fig. 4). On the other hand, while frequency calculations based on the DFT simulations do not suffer detection limits due to weak intensities or broad peak widths as do experiments, they do not include phonon-phonon interaction processes. Therefore, the broadband at 230 cm^{-1} is not reported in the calculated Raman spectra. Calculated Raman frequencies at the reference state (0 GPa static limit and 0 K) are reported in Table 2 together with the measured Raman frequencies on our "standard" rutile from Pohorje (peak positions of the two selected standards are

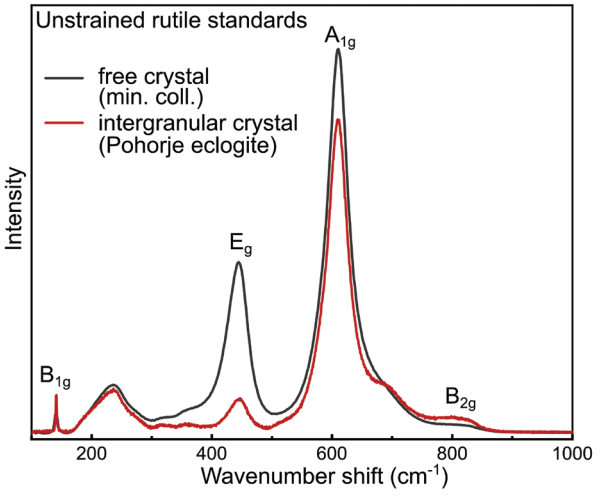

Figure 4. Raman spectra of the two natural rutile samples used as standards (rutile standard free crystal and intergranular rutile standard from the Pohorje eclogite). (Color online.)

TABLE 2. Frequencies (cm^{-1}) of the Raman-active modes of rutile

		This work		a	b	c	d	e	f
		calc	$exp_{Pohorje}$	Theoretical			Experimental		
T (K)		0	298	0	0	300	298	298	298
Symmetry	B_{1g}	163.98	141.6	137.0	130.0	169.0	143.0	143.0	143.0
	E_g	453.83	445.28	463.2	457.0	400.0	450.0	449.0	447.0
	A_{1g}	600.03	609.32	611.6	601.0	558.0	612.0	612.0	612.0
	B_{2g}	818.96	801.79	824.7	805.0	803.0	826.0	826.0	826.0

[a] Montanari and Harrison (2002).
[b] Mitev et al. (2010).
[c] Lan et al. (2012).
[d] Samara and Peercy (1973).
[e] Merle et al. (1980).
[f] Porto et al. (1967).

the same within the instrumental reproducibility of ~0.5 cm^{-1}) and literature data, which includes both theoretical and experimental data. Values of the calculated peak positions at 0 K differ slightly from the experimental results at room temperature due to the difference in temperature and the specifics of the calculation method. Ab initio hybrid HF/DFT calculations with the WC1LYP functional proved, on average, to be more effective in reproducing vibrational frequencies than other methods (Prencipe 2012, 2019). Frequencies calculated with WC1LYP for the E_g, A_{1g}, and B_{2g} **{{auth: ok?}}** modes are all within the range of experimental uncertainty. The significant discrepancy occurs with the experimental value of the B_{1g} mode because it is a low-frequency partially anharmonic mode, for which the computational uncertainties are larger.

Figure 5 displays the calculated $\Delta\omega$ (cm^{-1}) of the rutile Raman active modes (black solid lines) as a function of the two independent strain components. The E_g, A_{1g}, and B_{2g} modes display an increase of their vibrational frequencies with increase of negative strains. Their behavior could be seen to be almost linear within the studied strain field. According to the calculated displacement vectors from the DFT simulations, the E_g mode involves the vibrations along the **c** axis of the O_b atoms (Fig. 1) with the O_a atoms remaining fixed (one of the possible displacement geometries). The A_{1g} and the B_{2g} modes correspond to the movements of the oxygen atoms in the **a-b** planes, which includes Ti-O_b stretching and O_a-Ti-O_a scissoring in the <110> plane. The B_{1g} mode has an opposite behavior with respect to all of the other modes in that it displays negative shifts under compression (Fig. 5a). This anomalous behavior has already been described in the literature and is related to the pressure-induced structural phase transitions in rutile (Samara and Peercy 1973). The B_{1g} mode corresponds to rotational vibrations of the octahedra around the **c** axis. The directions of the rotations between adjacent octahedra are opposite to one another so this

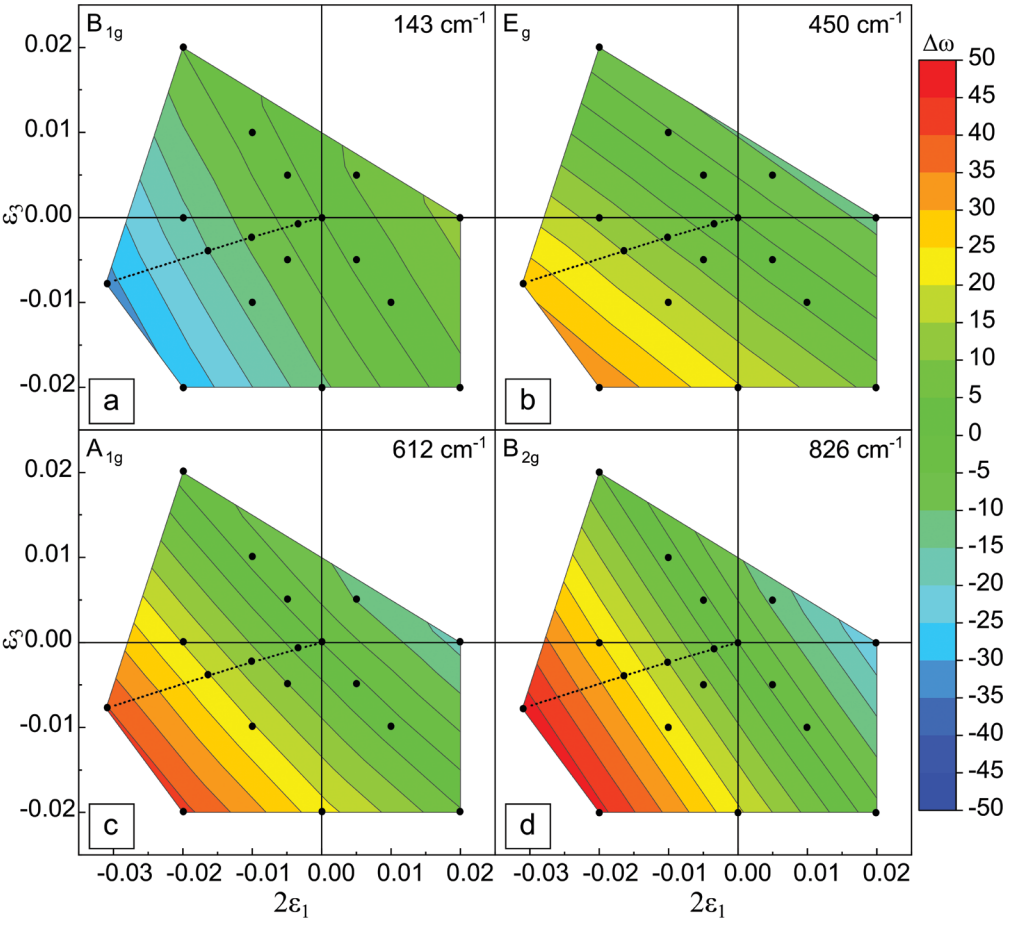

FIGURE 5. Calculated wavenumber shifts (cm^{-1}) of the Raman-active modes of rutile. Strains derived from the hydrostatic pressure simulations lie along the dotted line and represent pressure conditions of 0, 1, 3, 5, and 10 GPa from right to left. (Color online.)

mode represents a distortion of the octahedral chains involving only oxygen atom motions in the **a-b** plane. Softening of the B_{1g} optic mode drives a ferroelastic transition in which the symmetry is reduced from $P4_2/mnm$ to $Pnnm$ that also occurs at high pressures in several other compounds (e.g., stishovite, Carpenter et al. 2000) that have the rutile structure type.

Grüneisen tensor

Since the contour lines of equal $\Delta\omega$ (cm^{-1}) (black solid lines in the plots in Fig. 5) are equally spaced, straight, and parallel to one another, the dependence of all of the Raman modes of rutile on strain is linear. Therefore, the phonon-mode Grüneisen tensor approach can be applied to determine the Grüneisen tensor components for each Raman active mode. These will allow the strains in crystals to be determined from measured $\Delta\omega$ (cm^{-1}) and vice versa. The phonon-mode Grüneisen tensor γ^m is a second rank symmetric property tensor (e.g., Ziman 1960; Key 1967; Cantrell 1980; Angel et al. 2019) characteristic of each phonon mode *m*. Therefore, since only non-symmetry-breaking strains are considered, it obeys the symmetry constraints of the studied system. Rutile is tetragonal with non-symmetry-breaking strains restricted to $\varepsilon_1 = \varepsilon_2 \neq \varepsilon_3$ and, as a consequence, there are only two symmetry-independent Grüneisen components to be determined for each Raman active mode: γ_1^m and γ_1^m. Thus, the relationship between the wavenumber shifts of the Raman modes of rutile and the strains can be written in terms of the Grüneisen tensor as:

$$-\Delta\omega/\omega_0 = 2\gamma_1^m\varepsilon_1 + \gamma_1^m\varepsilon_3 \quad (1)$$

We determined the phonon-mode Grüneisen tensor components γ_1^m and γ_3^m for each Raman-active mode of rutile by a least-squares fit of the calculated $\Delta\omega$ (cm^{-1}) as a function of the strains. The reference values of ω_0 were taken from our measurements on the standard intergranular rutile from Pohorje (Slovenia).

To validate the calculated values of the symmetry-independent components of the mode Grüneisen tensors, we used them along with measured unit-cell strains under pressure to predict the Raman shift changes under pressure (Fig. 6). The available Raman data in the literature are only presented in the form of pressure derivatives ($\Delta\omega/P$ coefficients) and not measurements of individual data. The pressure interval of the experiments was 0–4 GPa (Nicol and Fong 1971; Samara and Peercy 1973), and in one case up to 40 GPa (Arashi 1992), but with a pressure medium of 4:1 methanol-ethanol mixture, which is hydrostatic only up to 9.8 GPa (Angel et al. 2007). We have a good agreement for the B_{1g} and A_{1g} modes and our calculations for the E_g mode are consistent with the experimental work done by Arashi (1992) over the larger interval of pressure. The difference in behavior of the calculated E_g mode from the experimental data of Nicol and Fong (1971) and Samara and Peercy (1973) might be due to its broader character and lower intensity compared to that of the A_{1g} mode.

Moreover, a linear behavior of the Raman modes with hydrostatic pressure is assumed when constant $\Delta\omega/P$ coefficients are used. However, the vibrational frequencies do not depend on the pressure but on the strains (Key 1967) and in our work were found to be linear with volume. The pressure dependence of the volume of rutile is described by the nonlinear Burch-Murnaghan equation of state of the third order (Zaffiro et al. 2019). Thus, fitting the $\Delta\omega$ (cm^{-1}) against pressure with a linear equation is not correct.

Discussion

Garnet is one of the most common host minerals for rutile and many other key inclusions such as quartz and zircon in metamorphic rocks. Quartz- and zircon-in-garnet elastic geobarometry has been successfully used to reconstruct *P-T* histories of metamorphic rocks (e.g., Gonzalez et al. 2019; Alvaro et al. 2020). However, calculations based on the equations of state of garnet (Milani et al. 2015) and rutile indicate that rutile inclusions trapped inside garnets at typical metamorphic conditions should exhibit negative residual pressures when measured at room conditions provided, they did not undergo some non-elastic process after entrapment (Zaffiro et al. 2019). Ab initio calculations did not reveal any anomalous behavior of the structure in the studied range of strains, which could result in a deviation of the behavior described by the EoS, nor any nonlinearity in the Grüneisen relationship between strains and Raman peak shifts (Eq. 1).

EoS calculations are confirmed by Raman measurements on both natural and synthetic samples. Bonazzi et al. (2019) synthesized at 3 GPa and 775 °C almost pure pyrope garnets with quartz and rutile inclusions. We performed Raman measurements on the rutile inclusions from these samples, and according to these and our optical observations, these synthetic rutile inclusions show no signs of residual pressure. Moreover, pyrope megablasts from the Dora Maira UHP locality (Chopin and Schertl 1999) are a good example of a natural garnet-rutile host inclusion system. Several rutile inclusions that are found in the same growth zones as coesite inclusions in these garnets do not show any sign of residual pressure: their Raman peaks are at the same wavenumbers as the free reference crystal, and there is no evidence for optical birefringence haloes in the surrounding garnet (N. Campomenosi, personal communication).

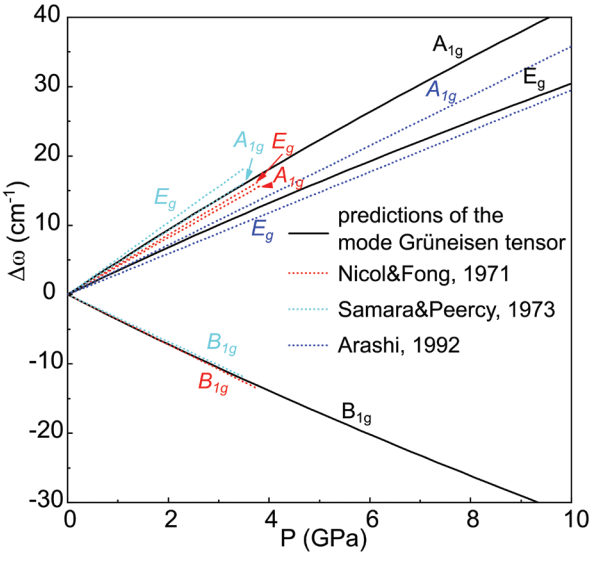

Figure 6. Predictions of the pressure-induced Raman shifts from the mode Grüneisen tensors (solid black lines) compared to $\Delta\omega/P$ coefficients from literature (colored dotted lines). (Color online.)

These observations are consistent with our simulation results and the thermodynamic calculations and indicate that rather than exhibiting negative pressures, which would imply that the rutile inclusions are bound to the host garnet crystal and stretched by it, the rutile inclusions are detached from the inclusion walls in the host garnet.

However, there are some rutile inclusions that appear to exhibit signs of residual pressure. For example, rutile inclusions in garnet from an eclogite from the Pohorje HP locality (Slovenia) are surrounded by a clearly distinguishable birefringence halo (Fig. 7).

This halo reflects the elastic deformation of the host garnet in the immediate vicinity of the inclusion due to its elastic relaxation (Campomenosi et al. 2020). The phenomenon of relaxation develops as a result of the differences between the thermoelastic properties of the host and inclusion phases that lead to the inclusion exhibiting a different pressure than the host. Therefore, birefringence haloes around these rutile inclusions when their host is at room pressure indicate that the inclusions are at some non-ambient pressure that cannot be caused solely by the contrast in elastic properties between rutile and garnet.

Optical and Raman spectroscopic studies of rutile inclusions in garnet from Pohorje revealed the presence of small amphibole crystals attached to each of the rutiles surrounded by a birefringence halo (e.g., Figs. 7a and 7d). Amphibole occurs as laminar crystals wrapping rutile grains, which makes it hard to detect and determine a volume fraction. Raman 3D imaging allowed us to estimate that an average volume fraction of amphibole in the inclusions exhibiting birefringence haloes is between 15 and 30% of the inclusion volume (rutile + amphibole) (Fig. 8). Electron microprobe analyses confirmed that the amphibole composition is close to the cummingtonite end-member (Online Material[1] Table OM1). The room-pressure bulk modulus of cummingtonite (Holland and Powell 2011) is 70 GPa, which is less than half the bulk modulus of pyrope. If the inclusion were pure amphibole, it would therefore exhibit a positive residual inclusion pressure (P_{inc}) when examined in our sections.

The elastic properties of mixed-phase inclusions have Reuss and Voigt bounds. We used the Reuss approximation as we expect the two phases to be under the same pressure rather than the same strain (Voigt approximation). The Reuss bulk modulus depends on the volume fractions x_1 and x_2 of both components:

$$K_{tot} = \left(\frac{x_1}{K_1} + \frac{x_2}{K_2} \right)^{-1} \quad (2)$$

On this basis, the presence of at least 14% in volume of cummingtonite is enough to reduce the bulk modulus (at ambient conditions) of the mixture to less than that of the garnet (Fig. 9). This makes the inclusion softer than the host and should lead to the development of a positive inclusion pressure upon exhumation.

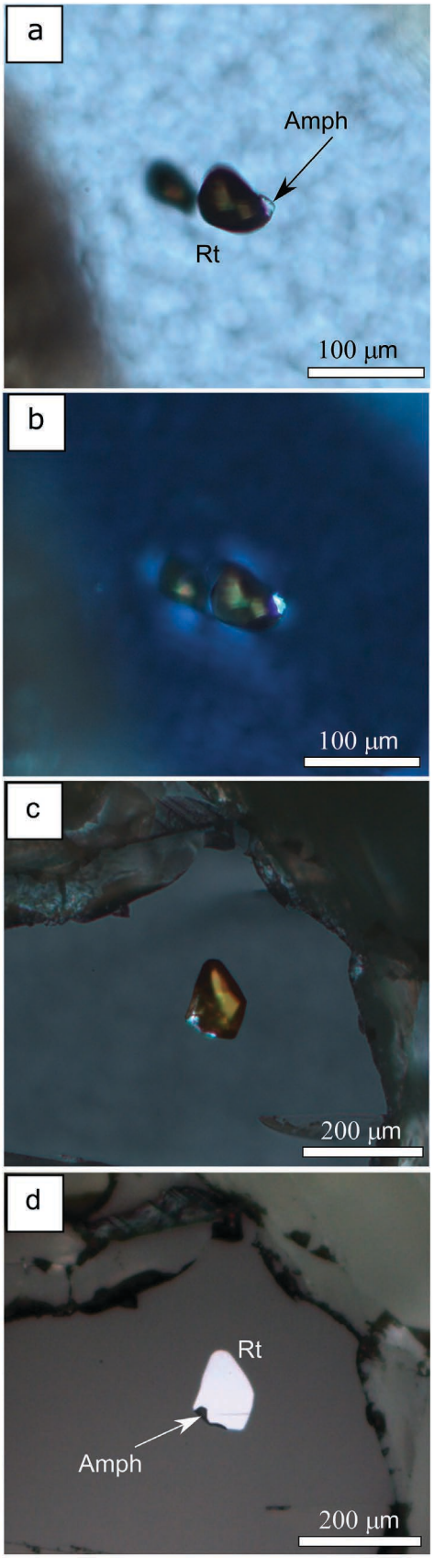

►**Figure 7.** Composite rutile + amphibole inclusions in garnet (eclogite from Pohorje massif). (**a** and **b**) Parallel-polarized light (PPL) and crossed-polarized light (XPL) microphotographs of the inclusions with the surrounding birefringent halo. (**c** and **d**) Surface inclusion in garnet [XPL and reflected light (RL) microphotographs]. Birefringent halo is absent on the image (**c**) because the stress is released as the inclusion is exposed [see Campomenosi et al. (2018) for details]. (Color online.)

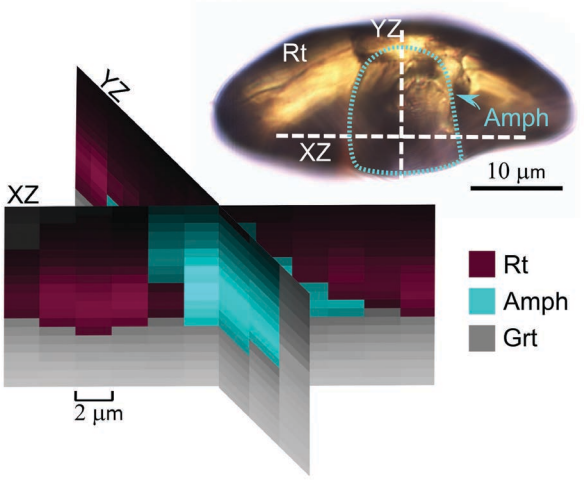

Figure 8. Raman imaging of a mixed rutile+amphibole inclusion along XZ and YZ planes. The blue area in the image indicates the presence of the 671 cm^{-1} characteristic peak of amphibole, while dark red and gray are related to the characteristic peaks at 141.6 and 917 cm^{-1} from rutile and garnet, respectively. (Color online.)

The value of the relaxed inclusion pressure for the multiple phase inclusion can be calculated using various approaches, for example, an average EoS weighted by molar fractions. But this method is inappropriate for the phases with contrasting elastic properties like rutile and amphibole because it does not account correctly for the differences in K' between the phases. Therefore, we developed a methodology that is implemented in the MPHASE utility of EosFit7c (Angel et al. 2014a), in which the volume of the mixture at all P and T is treated as the sum of the volumes of the individual phases calculated from their EoS weighted by their molar fractions. This calculation therefore treats the inclusion as a closed system of fixed composition under uniform stress. The orange and green curves in Figure 9 show variation of the P_{inc} value over the range of all possible amphibole fractions in a cummingtonite + rutile inclusion for the entrapment conditions of 3 GPa 800 °C and 2 GPa 600 °C. Different entrapment conditions within the range of regional metamorphism lead to a different slope of this curve, but it always crosses the point of zero P_{inc} at ~0.14 volume fraction of the amphibole component. A mixture of ~14 vol% of a cummingtonite and ~86% of a rutile has the same bulk modulus as a pyrope garnet, therefore P_{inc} should be approximately zero in the interval from 13 to 15 vol% of cummingtonite (variation of 1 vol% for the different entrapment conditions). Inverse calculations of the entrapment conditions of such composite inclusions therefore require a precise measurement of the volume fractions of the phases and the value of the P_{inc}, as well as the composition of the amphibole as the bulk modulus and EoS of amphiboles varies with composition.

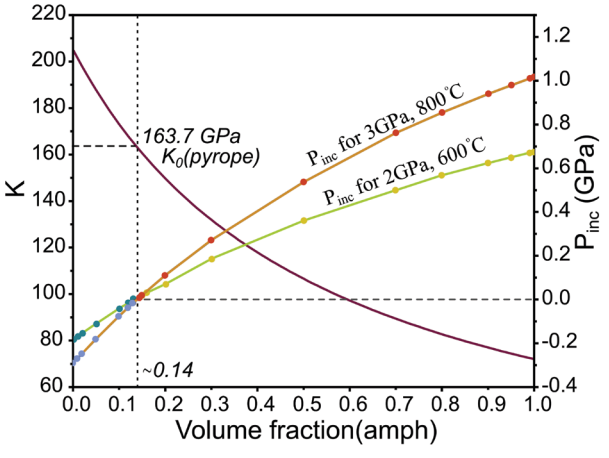

Figure 9. Bulk modulus (red) and P_{inc} (orange and green) curves at room conditions of rutile plus cummingtonite mixtures as a function of volume fraction of the amphibole. Negative P_{inc} values are indicated with blue dots, while positive values with red and yellow dots. The bulk modulus curve corresponds to the Reuss expression for the bulk modulus of the two-phase mixture. Values of the P_{inc} are calculated for the entrapment condition at 3 GPa 800 °C and at 2 GPa 600 °C as an example. The volume fraction of the amphibole (0.14) leading to a zero P_{inc} is also the composition for which the bulk modulus of the inclusion is equal to that of the pyrope host. (Color online.)

The multi-phase inclusion from Pohorje eclogite with 30 vol% of cummingtonite amphibole can exhibit up to 0.28 GPa of a residual pressure according to the calculated P_{inc} curves, which is consistent with the presence of birefringence haloes in the host around these inclusions. Changes in the Raman peak positions ($\Delta\omega$, cm^{-1}) in the rutile spectrum corresponding to this pressure however are impossible to resolve as they are less than the typical measurement uncertainties. However, amphibole Raman $\Delta\omega$ (cm^{-1}) could be used to detect the residual pressure, but for this a reliable pressure calibration is needed.

Implications

Ab initio calculations of elastic and vibrational properties of rutile predicted a linear response of its structural parameters and vibrational frequencies to strains. We determined the symmetry-independent components of the phonon-mode Grüneisen tensors for the rutile Raman active modes that can be used in Raman elastic geobarometry calculations. Our DFT calculations succeeded in predicting the anomalous behavior of the soft B_{1g} mode. Thus, we confirm that a compressional strain causes a negative shift of the lowest-frequency Raman mode (141.6 cm^{-1}) of rutile.

Thermodynamic calculations predict a negative P_{inc} for rutile inclusions entrapped in garnet at HP conditions; therefore, we would expect a positive peak shift for the B_{1g} mode and negative peak shifts for the other Raman modes in rutile. However, this behavior has not been observed so far, and pure rutile inclusions have zero pressures in both natural and synthetic samples. On the other hand, we demonstrated that detecting a positive P_{inc} in some rutile inclusions is theoretically possible due to softening of the overall inclusion bulk modulus. Extensive radiation damage to rutile or the presence of a second phase, softer than rutile

Table 3. Symmetry-independent components of the Grüneisen tensors of rutile at 300 K

	ω_0	γ_1	γ_3
B_{1g}	141.6	–5.64 (16)	–4.23(21)
E_g	445.28	1.45 (2)	2.38 (2)
A_{1g}	609.32	1.57 (3)	1.88 (4)
B_{2g}	801.79	1.57 (1)	1.32 (1)

{{auth: Table 3 needs a callout in the text or delete}}

and garnet (e.g., amphibole), can modify the bulk modulus of the inclusion enough to reverse the contrast of elastic properties to the host garnet. Here, we described a method to calculate the elastic properties of multi-phase inclusions with the EoSFit-7c software (Angel et al. 2014a). The results of our calculations can be used as a control for the presence of plastic deformation, radiation damage, or the vicinity of another phase in**{{auth: ok?}}** the case where a residual pressure in the inclusion or a birefringence halo is detected.

Elastic geobarometry can still be used for rutile inclusions in other hosts with more contrasting elastic properties, such as quartz or diamond (Angel et al. 2015, 2017). Even though quartz is softer than rutile at room P and T, a window of positive P_{inc} occurs for rutile inclusions entrapped at low P (up to 0.7 GPa) and medium-high T (200–700 °C) conditions under the zero-pressure entrapment isomeke (Online Material[1] Fig. OM1a). Rutile inclusions in diamond will exhibit positive P_{inc} if entrapped above the zero isomeke (Online Material[1] Fig. OM1b) corresponding to low T and high P conditions. For example, a P_{inc} of 1 GPa, corresponding to a 0.4% volume strain, will cause the Raman modes B_{1g}, E_g, A_{1g}, and B_{2g} to shift –3.2, 3.1, 4.2, and 5.2 cm^{-1}, respectively. These $\Delta\omega$ values are significantly above the measurement uncertainties caused by line broadening and thus residual pressures of rutile inclusions in diamonds could be detected by Raman measurements.

In cases of a positive inclusion pressure, a strained rutile inclusion will display a negative $\Delta\omega$ cm^{-1} for the B_{1g} mode and positive $\Delta\omega$ cm^{-1} for the other Raman modes. However, it is important to remember that in anisotropic hosts the differences from the hydrostatic calibration depend on the reciprocal orientation of host and inclusion. The problem of orientation is partially solved in the case of rutile inclusions that have exsolved from the host phase. They are usually tiny needles of acicular rutile, oriented along crystallographic axes of the host phase. The process of the decomposition of a Ti-rich solid solution leads to the formation of coherent inclusions (e.g., Zhang et al. 2003; Proyer et al. 2013). Understanding the influence of this coherency on the resulting strains in a host-inclusion system is now possible with an application of these newly calculated symmetry-independent components of the phonon-mode Grüneisen tensors.

Acknowledgments and Funding

The authors thank Hugo Van Schrojenstein Lantman for the samples from Pohorje and electron microprobe analyses and Mattia Bonazzi and Nicola Campomenosi for discussions about Raman data of rutile inclusions in garnet. This project received funding from the European Research Council under the European Union's Horizon 2020 research and innovation program grant agreement 714936 TRUE DEPTHS to Matteo Alvaro.

References cited

Abrahams, S.C., and Bernstein, J.L. (1971) Rutile: Normal probability plot analysis and accurate measurement of crystal structure. The Journal of Chemical Physics, 55, 3206–3211.

Alvaro, M., Mazzucchelli, M.L., Angel, R.J., Murri, M., Campomenosi, N., Scambelluri, M., Nestola, F., Korsakov, A., Tomilenko, A.A., Marone, F., and others. (2020) Fossil subduction recorded by quartz from the coesite stability field. Geology, 48, 24–28.

Angel, R.J., Bujak, M., Zhao, J., Gatta, G.D., and Jacobsen, S.D. (2007) Effective hydrostatic limits of pressure media for high-pressure crystallographic studies. Journal of Applied Crystallography, 40, 26–32.

Angel, R.J., Alvaro, M., and Gonzalez-Platas, J. (2014a) EosFit7c and a Fortran module (library) for equation of state calculations. Zeitschrift für Kristallographie: Crystalline Materials, 229, 405–419.

Angel, R.J., Mazzucchelli, M.L., Alvaro, M., Nimis, P., and Nestola, F. (2014b) Geobarometry from host-inclusion systems: The role of elastic relaxation. American Mineralogist, 99, 2146–2149.

Angel, R.J., Alvaro, M., Nestola, F., and Mazzucchelli, M.L. (2015) Diamond thermoelastic properties and implications for determining the pressure of formation of diamond-inclusion systems. Russian Geology and Geophysics, 56, 211–220.

Angel, R.J., Alvaro, M., Miletich, R., and Nestola, F. (2017) A simple and generalised *P-T-V* EoS for continuous phase transitions, implemented in EosFit and applied to quartz. Contributions to Mineralogy and Petrology, 172, 29.

Angel, R.J., Murri, M., Mihailova, B., and Alvaro, M. (2019) Stress, strain and Raman shifts. Zeitschrift für Kristallographie: Crystalline Materials, 234, 129–140.

Angel, R.J., Alvaro, M., Schmid-Beurmann, P., and Kroll, H. (2020) Commentary on "Constraints on the Equations of State of stiff anisotropic minerals: rutile, and the implications for rutile elastic barometry" [Mineralogical Magazine 83 (2019) pp. 339–347]. Mineralogical Magazine, 84, 339–347.

Arashi, H. (1992) Raman spectroscopic study of the pressure-induced phase transition in TiO_2. Journal of Physics and Chemistry of Solids, 53, 355–359.

Bonazzi, M., Tumiati, S., Thomas, J.B., Angel, R.J., and Alvaro, M. (2019) Assessment of the reliability of elastic geobarometry with quartz inclusions. Lithos, 350-351, 105201.

Burdett, J.K., Hughbanks, T., Miller, G.J., Richardson, J.W., and Smith, J.V. (1987) Structural-electronic relationships in inorganic solids: powder neutron diffraction studies of the rutile and anatase polymorphs of titanium dioxide at 15 and 295 K. Journal of the American Chemical Society, 109, 3639–3646.

Campomenosi, N., Mazzucchelli, M.L., Mihailova, B., Scambelluri, M., Angel, R.J., Nestola, F., Reali, A., and Alvaro, M. (2018) How geometry and anisotropy affect residual strain in host-inclusion systems: Coupling experimental and numerical approaches. American Mineralogist, 103, 2032–2035.

Campomenosi, N., Mazzucchelli, M.L., Mihailova, B.D., Angel, R.J., and Alvaro, M. (2020) Using polarized Raman spectroscopy to study the stress gradient in mineral systems with anomalous birefringence. Contributions to Mineralogy and Petrology, 175, 16.

Cantrell, J.H. (1980) Generalized Grüneisen tensor from solid nonlinearity parameters. Physical Review B, 21, 4191–4195.

Carpenter, M.A., Hemley, R.J., and Mao, H. (2000) High-pressure elasticity of stishovite and the $P4_2/mnm \rightleftharpoons Pnnm$ phase transition. Journal of Geophysical Research: Solid Earth, 105, 10807–10816.

Carruzzo, S., Clarke, D.B., Pelrine, K.M., and MacDonald, M.A. (2006) Texture, composition, and origin of rutile in the South Mountain batholith, Nova Scotia. Canadian Mineralogist, 44, 715–729.

Černý, P., Novak, M., Chapman, R., and Ferreira, K.J. (2007) Subsolidus behavior of niobian rutile from the Pisek region, Czech Republic: A model for exsolution in W^- and Fe^{2+}>>Fe^{3+}-rich phases. Journal of Geosciences, 52, 143–159.

Černý, P., Chapman, R., Simmons, W.B., and Chackowsky, L.E. (2015) Niobian rutile from the McGuire granitic pegmatite, Park County, Colorado: Solid solution, exsolution, and oxidation. American Mineralogist, 84, 754–763.

Chopin, C., and Schertl, H.-P. (1999) The UHP Unit in the Dora-Maira Massif, Western Alps. International Geology Review, 41, 765–780.

Civalleri, B., D'Arco, Ph., Orlando, R., Saunders, V.R., and Dovesi, R. (2001) Hartree-Fock geometry optimisation of periodic systems with the Crystal code. Chemical Physics Letters, 348, 131–138.

Demuth, T., Jeanvoine, Y., Hafner, J., and Ángyán, J.G. (1999) Polymorphism in silica studied in the local density and generalized-gradient approximations. Journal of Physics: Condensed Matter, 11, 3833–3874.

Dovesi, R., Saunders, V.R., Roetti, C., Orlando, R., Zicovich Wilson, C.M., Pascale, F., Civalleri, B., Doll, K., Harrison, N.M., Bush, I.J., and others (2014) CRYSTAL14.**{{AU: need publisher's name and location, at least a host instiution -- ditto for next reference}}**

——— (2018a) CRYSTAL17 User's Manual, 461 p.

Dovesi, R., Erba, A., Orlando, R., Zicovich-Wilson, C.M., Civalleri, B., Maschio, L., Rérat, M., Casassa, S., Baima, J., Salustro, S., and others (2018b) Quantum-mechanical condensed matter simulations with CRYSTAL. WIREs Computational Molecular Science, 8, 1360.

Erba, A., and Dovesi, R. (2013) Photoelasticity of crystals from theoretical simulations. Physical Review B, 88, 045121.

Ferry, J.M., and Watson, E.B. (2007) New thermodynamic models and revised calibrations for the Ti-in-zircon and Zr-in-rutile thermometers. Contributions to Mineralogy and Petrology, 154, 429–437.

Gonzalez, J.P., Thomas, J.B., Baldwin, S.L., and Alvaro, M. (2019) Quartz-in-garnet and Ti-in-quartz thermobarometry: Methodology and first application to a quartzofeldspathic gneiss from eastern Papua New Guinea. Journal of Metamorphic Geology, 37, 1193–1208.

Henderson, C.M.B., Knight, K.S., and Lennie, A.R. (2009) Temperature dependence of rutile (TiO_2) and geikielite ($MgTiO_3$) structures determined using neutron powder diffraction. The Open Mineralogy Journal, 3, 1–11.

Holland, T.J.B., and Powell, R. (2011) An improved and extended internally consistent thermodynamic dataset for phases of petrological interest, involving a new equation of state for solids. Journal of Metamorphic Geology, 29, 333–383.

Key, S.W. (1967) Grüneisen tensor for anisotropic materials. Journal of Applied Physics, 38, 2923–2928.
Kimizuka, H., Kaburaki, H., and Kogure, Y. (2003) Molecular-dynamics study of the high-temperature elasticity of quartz above the α-β phase transition. Physical Review B, 67, 024105.
Lan, T., Tang, X., and Fultz, B. (2012) Phonon anharmonicity of rutile TiO_2 studied by Raman spectrometry and molecular dynamics simulations. Physical Review B, 85, 094305.
Lan, T., Li, C.W., Hellman, O., Kim, D.S., Muñoz, J.A., Smith, H., Abernathy, D.L., and Fultz, B. (2015) Phonon quarticity induced by changes in phonon-tracked hybridization during lattice expansion and its stabilization of rutile TiO_2. Physical Review B, 92, 054304.
Lee, C., Yang, W., and Parr, R.G. (1988) Development of the Colle-Salvetti correlation-energy formula into a functional of the electron density. Physical Review B, 37, 785–789.
Meinhold, G. (2010) Rutile and its applications in earth sciences. Earth-Science Reviews, 102, 1–28.
Merle, P., Pascual, J., Camassel, J., and Mathieu, H. (1980) Uniaxial-stress dependence of the first-order Raman spectrum of rutile. I. Experiments. Physical Review B, 21, 1617–1626.
Milani, S., Nestola, F., Alvaro, M., Pasqual, D., Mazzucchelli, M.L., Domeneghetti, M.C., and Geiger, C.A. (2015) Diamond-garnet geobarometry: The role of garnet compressibility and expansivity. Lithos, 227, 140–147.
Mitev, P.D., Hermansson, K., Montanari, B., and Refson, K. (2010) Soft modes in strained and unstrained rutile TiO_2. Physical Review B, 81, 134303.
Momma, K., and Izumi, F. (2008) VESTA: A three-dimensional visualization system for electronic and structural analysis. Journal of Applied Crystallography, 41, 653–658.
Monkhorst, H.J., and Pack, J.D. (1976) Special points for Brillouin-zone integrations. Physical Review B, 13, 5188–5192.
Montanari, B., and Harrison, N.M. (2002) Lattice dynamics of TiO_2 rutile: Influence of gradient corrections in density functional calculations. Chemical Physics Letters, 364, 528–534.
Murri, M., Mazzucchelli, M.L., Campomenosi, N., Korsakov, A.V., Prencipe, M., Mihailova, B.D., Scambelluri, M., Angel, R.J., and Alvaro, M. (2018) Raman elastic geobarometry for anisotropic mineral inclusions. American Mineralogist, 103, 1869–1872.
Murri, M., Alvaro, M., Angel, R.J., Prencipe, M., and Mihailova, B.D. (2019) The effects of non-hydrostatic stress on the structure and properties of alpha-quartz. Physics and Chemistry of Minerals, 46, 487–499.
Nicol, M., and Fong, M.Y. (1971) Raman spectrum and polymorphism of titanium dioxide at high pressures. The Journal of Chemical Physics, 54, 3167–3170.
Pascale, F., Zicovich-Wilson, C.M., Gejo, F.L., Civalleri, B., Orlando, R., and Dovesi, R. (2004) The calculation of the vibrational frequencies of crystalline compounds and its implementation in the CRYSTAL code. Journal of Computational Chemistry, 25, 888–897.
Peintinger, M.F., Oliveira, D.V., and Bredow, T. (2013) Consistent Gaussian basis sets of triple-zeta valence with polarization quality for solid-state calculations. Journal of Computational Chemistry, 34, 451–459.
Porto, S.P.S., Fleury, P.A., and Damen, T.C. (1967) Raman spectra of TiO_2, MgF_2, ZnF_2, FeF_2, and MnF_2. Physical Review, 154, 522–526.
Prencipe, M. (2012) Simulation of vibrational spectra of crystals by ab initio calculations: An invaluable aid in the assignment and interpretation of the Raman signals. The case of jadeite ($NaAlSi_2O_6$). Journal of Raman Spectroscopy, 43, 1567–1569.
——— (2019) Quantum mechanics in Earth sciences: a one-century-old story. Rendiconti Lincei. Scienze Fisiche e Naturali, 30, 239–259.
Prencipe, M., Scanavino, I., Nestola, F., Merlini, M., Civalleri, B., Bruno, M., and Dovesi, R. (2011) High-pressure thermo-elastic properties of beryl ($Al_4Be_6Si_{12}O_{36}$) from ab initio calculations, and observations about the source of thermal expansion. Physics and Chemistry of Minerals, 38, 223–239.
Proyer, A., Habler, G., Abart, R., Wirth, R., Krenn, K., and Hoinkes, G. (2013) TiO_2 exsolution from garnet by open-system precipitation: Evidence from crystallographic and shape preferred orientation of rutile inclusions. Contributions to Mineralogy and Petrology, 166, 211–234.
Rosenfeld, J.L., and Chase, A.B. (1961) Pressure and temperature of crystallization from elastic effects around solid inclusions in minerals? American Journal of Science, 259, 519–541.
Samara, G.A., and Peercy, P.S. (1973) Pressure and temperature dependence of the static dielectric constants and Raman spectra of TiO_2 (rutile). Physical Review B, 7, 1131–1148.
Stangarone, C., Tribaudino, M., Prencipe, M., and Lottici, P.P. (2016) Raman modes in *Pbca* enstatite ($Mg_2Si_2O_6$): An assignment by quantum mechanical calculation to interpret experimental results. Journal of Raman Spectroscopy, 47, 1247–1258.
Stangarone, C., Angel, R.J., Prencipe, M., Campomenosi, N., Mihailova, B., and Alvaro, M. (2019) Measurement of strains in zircon inclusions by Raman spectroscopy. European Journal of Mineralogy, 685–694.
Sugiyama, K., and Takéuchi, Y. (2015) The crystal structure of rutile as a function of temperature up to 1600 °C. Zeitschrift für Kristallographie: Crystalline Materials, 194, 305–314.
Vrabec, M., Janák, M., Froitzheim, N., and De Hoog, J.C.M. (2012) Phase relations during peak metamorphism and decompression of the UHP kyanite eclogites, Pohorje Mountains (Eastern Alps, Slovenia). Lithos, 144-145, 40–55.
Wu, Z., and Cohen, R.E. (2006) More accurate generalized gradient approximation for solids. Physical Review B, 73, 235116.
Zaffiro, G., Angel, R.J., and Alvaro, M. (2019) Constraints on the Equations of State of stiff anisotropic minerals: Rutile, and the implications for rutile elastic barometry. Mineralogical Magazine, 83, 339–347.
Zhang, R.Y., Zhai, S.M., Fei, Y.W., and Liou, J.G. (2003) Titanium solubility in coexisting garnet and clinopyroxene at very high pressure: The significance of exsolved rutile in garnet. Earth and Planetary Science Letters, 216, 591–601.
Ziman, J.M. (1960) Electrons and phonons, the International Series of Monographs on Physics. Oxford University, London, U.K.

Manuscript received May 18, 2020
Manuscript accepted November 11, 2020
Manuscript handled by Zhicheng Jing

Endnote:

[1]Deposit item AM-21-107618, Online Materials. Deposit items are free to all readers and found on the MSA website, via the specific issue's Table of Contents (go to http://www.minsocam.org/MSA/AmMin/TOC/2021/Oct2021_data/Oct2021_data.html). The CIF has been peer-reviewed by our Technical Editors.